# The Stomatopod Dactyl Club: A Formidable Damage-Tolerant Biological Hammer

James C. Weaver,[1]* Garrett W. Milliron,[2]* Ali Miserez,[3]* Kenneth Evans-Lutterodt,[4] Steven Herrera,[2] Isaias Gallana,[5] William J. Mershon,[6] Brook Swanson,[7] Pablo Zavattieri,[5] Elaine DiMasi,[4] David Kisailus[2]†

Nature has evolved efficient strategies to synthesize complex mineralized structures that exhibit exceptional damage tolerance. One such example is found in the hypermineralized hammer-like dactyl clubs of the stomatopods, a group of highly aggressive marine crustaceans. The dactyl clubs from one species, *Odontodactylus scyllarus*, exhibit an impressive set of characteristics adapted for surviving high-velocity impacts on the heavily mineralized prey on which they feed. Consisting of a multiphase composite of oriented crystalline hydroxyapatite and amorphous calcium phosphate and carbonate, in conjunction with a highly expanded helicoidal organization of the fibrillar chitinous organic matrix, these structures display several effective lines of defense against catastrophic failure during repetitive high-energy loading events.

The stomatopods are an ancient group of marine tropical and subtropical crustaceans with a fossil record that dates back more than 300 million years (*1*). Modern representatives reach lengths of nearly 40 cm, although most species are appreciably smaller (e.g., 15 cm). To the casual observer, they superficially resemble heavily armored caterpillars, and the group is best known for their complex visual systems (*2*), solitary nature, and aggressive hunting strategies (*3*). In stomatopods, the second pair of thoracic appendages is highly modified and specifically adapted for powerful close-range combat. The dactyl modifications (the terminal segment) of these appendages divide the group into those that either hunt by impaling their prey with spear-like structures or those that smash them with a powerful blow from a heavily mineralized club (*4*). This robust hammer-like composite structure can inflict considerable damage after impact with a wide variety of heavily mineralized biological structures (e.g., mollusk shells, crab exoskeletons, the skulls of small fish, and the occasional weary fisherman) (*5*). Notably, many of these prey items represent model systems for the study of tough and damage-tolerant biological materials (*6*, *7*), and investigations into their micro- and nanoarchitectural features have provided critical insight into the design of robust synthetic analogs (*8*, *9*). This observation highlights the unique structure and impressive performance of the stomatopod dactyl club, and the important lessons that can be learned from its investigation.

We report a comprehensive study of the structural complexity and mechanical properties of the dactyl clubs of *Odontodactylus scyllarus*, a common reef-associated stomatopod from the tropical Indo-Pacific (*10*). As described by Patek *et al.* (*11*), these formidable structures are capable of accelerations to 10,400*g* and speeds of 23 m/s from a stationary position. Their rapid strike can generate cavitation bubbles between the appendage and their prey, with the collapse of these bubbles producing high stresses at the contact point, in addition to the instantaneous forces of ≥700 N resulting from the direct impact (*11*). Despite these large loads, the dactyl clubs are extremely damage tolerant and can withstand thousands of highly energetic blows (*12*) before being replaced during periodic molting events.

**Structural and micromechanical characterization.** At the macroscale, the club comprises the two terminal segments (the propodus and the dactyl) of the second thoracic appendage (Fig. 1, A to C). For deployment during a striking event, the dactyl is folded back into a groove in the propodus to form the functional club. Whole-body microcomputed tomographic analysis (Fig. 1D) of *O. scyllarus* reveals that the dactyl club is the most electron-dense region of the stomatopod exoskeleton, being up to five times as thick as its adjacent appendages. When viewed in a transverse cross section, the club can be divided into three distinct regions (Fig. 1, E and F): the impact region, the periodic region, and the striated region.

Nanoindentation and energy-dispersive spectroscopy (EDS) measurements (Fig. 2, A to C) of sectioned clubs reveal a distinct correlation between the extent of mineralization and their corresponding mechanical properties. EDS measurements tracking regiospecific elemental distributions reveal decreasing phosphorus and calcium concentrations from the impact surface to the interior of the dactyl club and a concomitant increase in carbon and magnesium throughout the same region. Although there is an abrupt step-like decrease in calcium concentration through the transition from the impact region to the periodic region, the phosphorous concentration decreases in a gradient-like fashion (Fig. 2C). These results indicate a biphasic mineral system, with the impact region dominated by calcium phosphate and the remainder of the club likely consisting of a mixture of calcium phosphate and calcium carbonate. Large-area nanoindentation maps and high-resolution line scans through the midline of the dactyl club (Fig. 2B and fig. S1) reveal that the highest phosphorus content region also exhibits the highest hardness and modulus, which is consistent with previous single-point measurements made on a related species (*13*). In addition, there is a direct correlation between the extent of mineralization and the dry versus hydrated values obtained from the nanoindentation studies. Based on these measurements, the club can be divided into three mechanically distinct domains: (i) the hard outermost region of the club (the impact surface), measuring ~50 to 70 μm thick and exhibiting modulus values of 65 to 70 GPa (with no appreciable differences in measured values between dry and hydrated conditions); (ii) a sharp transitional zone with an abrupt decrease in modulus within the bulk of the impact region (45 GPa dry versus 35 GPa hydrated); and (iii) a periodic region with oscillating minima and maxima modulus values of 10 and 25 GPa (3 to 8 GPa under hydrated conditions).

Cross-sectional synchrotron microdiffraction mapping (Fig. 3) reveals hydroxyapatite as the dominant mineral phase within the impact region. X-ray diffraction patterns acquired from this region reveal that, compared to the apatitic mineral phase found in bovine bone (*14*), the dactyl club hydroxyapatite exhibits a higher degree of crystallinity, as evidenced by the distinct separation of the (211), (112), and (300) reflections (Fig. 3B). By contrast, the periodic region lacks any defined crystallinity and is instead dominated by an amorphous mineral phase, a feature common to other groups of crustaceans (*15*). This observation is also consistent with the elevated magnesium concentrations of the periodic region, which has been shown to aid in the stabilization of amorphous calcium carbonates in other biological systems (*16*, *17*). Further analysis of the synchrotron mapping data reveals that the hydroxyapatite crystallites exhibit a preferred orientation with the (002) lattice planes

[1]Wyss Institute for Biologically Inspired Engineering, Harvard University, Cambridge, MA 01238, USA. [2]Department of Chemical and Environmental Engineering, University of California, Riverside, Riverside, CA 92521, USA. [3]School of Materials Science and Engineering and School of Biological Sciences, Nanyang Technological University, Singapore 639798. [4]National Synchrotron Light Source, Brookhaven National Laboratory, Upton, NY 11973, USA. [5]College of Engineering, Purdue University, West Lafayette, IN 47907, USA. [6]Tescan-USA, Cranberry Township, PA 16066, USA. [7]Biology Department, Gonzaga University, Spokane, WA 99258, USA.

*These authors contributed equally to this work.
†To whom correspondence should be addressed. E-mail: david@engr.ucr.edu

oriented parallel to the impact surface (Fig. 3C), a theme observed throughout the impact region.

Underlying the mineral phases is the chitinous organic matrix, which exhibits a characteristic helicoidal organization (Fig. 4). The sheets of locally parallel chitin fibrils are stacked upon each other such that each sheet is skewed by an angle from the sheet below it. This constant difference in angle between neighboring sheets ultimately produces a rotation of 180°, defining a characteristic wavelength and a superlayer. These superlayers are easily identified by scanning electron microscopy (SEM) or optical microscopy (Figs. 1F and 2A) and decrease in thickness from the club exterior to the interior in a linear fashion. Each superlayer follows the club's contours (Fig. 1E), defining (i) the medial zone beneath the impact region and (ii) the lateral zone along the sides of the club. Compared to other helicoidal biocomposites (*18–20*), the highly expanded helicoidal periodicity of the stomatopod dactyl club makes it an ideal system for synchrotron fiber diffraction studies that have been previously resolution limited in other crustacean species by the x-ray beam spot size (*21*). Texture analysis of the helicoidal ultrastructure using a microdiffraction beam line with a spot size of 5 μm by 5 μm is shown in Fig. 4, D and E, using the *d*-spacing of the (110) peaks of α-chitin (*22–24*).

**Dynamic finite element analysis.** To gain insights into the damage tolerance of the club, we performed dynamic finite element modeling (DFEM) of a striking event against a solid target (Fig. 5, A to C), with the mesh following the complex macroscale geometry of the dactyl and propodus (Fig. 5A). To accurately compare the obtained results with previous data from Patek and Caldwell (*11*), we modeled the target as a steel cylinder ($E$ = 200 GPa) with 1 mm thickness and 5 mm radius, and based the impact velocity (20 m/s) on their measured final velocity (see supplementary materials for details). We validated the simulations by comparing the computed strike force with the measured one, which gave a comparable value of 550 to 575 N (versus 693 ± 174 N in the experiments). Additional simulations were performed to assess the influence of isotropic damage (cracking) or softening (plasticity) on the stress distribution, with the tensile load to initiate cracking or plasticity ranging from 10 to 50 MPa. Although the impact energy absorbed by microcracking or microplasticity reduced the strike force by ~15%, the critical stress values and their overall distribution in the impact region did not change substantially.

The dynamic evolution of the maximum principal stress ($\sigma_{max}$) following contact (Fig. 5B) reveals that the impact wave travels through the entire club and reaches the end of the dactyl ~2.5 μs after contact, before being transmitted through the propodus. Because these simulations predict that the maximum values of $\sigma_{max}$ are achieved 2 μs after impact, they imply that the propodus has no appreciable effect on the distribution of these critical stress values. Analysis of the maximum stress components at 2 μs after impact (Fig. 5C) include (i) the hydrostatic pressure $\sigma^H$ (blue tones), (ii) the in-plane maximum principal stress $\sigma^{IP}_{max}$ (green tones), and (iii) the out-of-plane maximum principal stress, $\sigma^{OP}_{max}$ (red tones). These computations imply that the club is subjected to extremely high hydrostatic compressive stresses, with $\sigma^H$ up to 4 GPa reached within a 0.2-mm radius from the contact point. For comparison, the compressive strength of engineering ceramics such as zirconia or silicon carbide is on the order of 2 to 3.5 GPa (*25*). Because the dactyl club does not fail catastrophically during impact, this highlights its ability to sustain extremely high levels of localized impact pressure.

Internal damage can follow the direction of conical stresses (in the plane of the club's long axis) or radial stresses (orthogonal to the computational plane), with crack initiation governed by $\sigma^{IP}_{max}$ or $\sigma^{OP}_{max}$, respectively. The maximum values of $\sigma^{IP}_{max}$ are located beneath the impact surface and close to the interface with the periodic region, reaching values well over 100 MPa, which

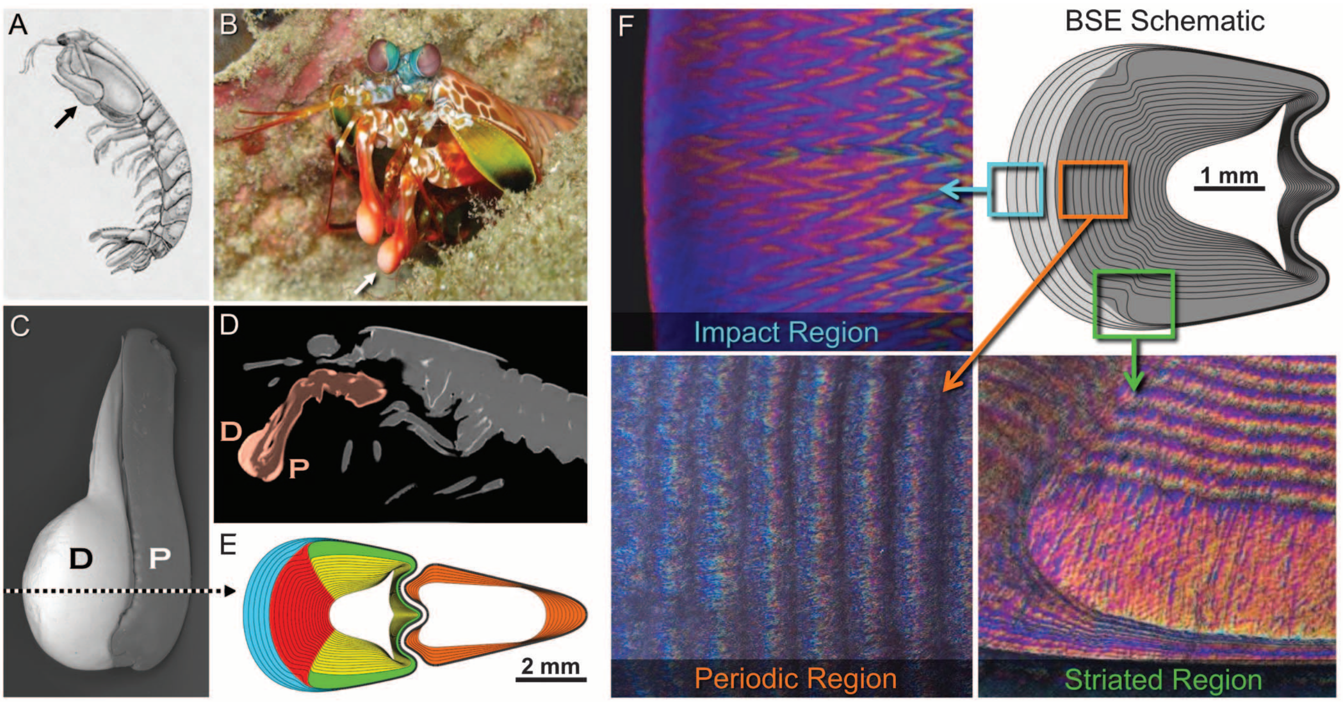


**Fig. 1.** Morphological features of the stomatopod dactyl club. (**A**) A generalized stomatopod body plan and (**B**) a magnified view of the anterior end of *O. scyllarus*. The arrows denote the location of the dactyl club's impact surface. (**C**) Backscattered scanning electron micrograph of the club's external morphology and (**D**) a microcomputed tomographic longitudinal section through the anterior half of a complete specimen showing the constituent dactyl (D) and propodus (P) segments, revealing their differences in electron density (the second thoracic appendage with its terminal dactyl club modification is highlighted in red). (**E**) Cross-sectional analysis of the club illustrates the three distinct structural domains: (i) The impact region (blue), (ii) the periodic region [further subdivided into two discrete zones: medial (red) and lateral (yellow)], and (iii) the striated region (green). The periodic region of the propodus is shown in orange. (**F**) Optical micrographs, revealing the buckled rotated plywood structural motif of the impact region, the pseudo-laminations of the periodic region, and the thickened circumferential band with parallel chitin fibers in the striated region [(A) adapted from (*37*), (B) courtesy of S. Baron, and (D) courtesy of DigiMorph.org].

correspond to the tensile strengths of monolithic ceramics. Conical cracks would hence be expected to nucleate near the impact/periodic region interface. The periodic region, which in contrast has a lower mineral content, is subjected to lower in-plane stresses. The highest values of $\sigma_{max}^{OP}$ are highly localized beneath the initial point of impact, reaching values that can exceed 300 MPa, suggesting that radial cracks are likely to also nucleate near the impact/periodic region interface. Most of the club is subjected to moderate $\sigma_{max}^{OP}$ values (10 to 100 MPa), implying that radial cracks are less likely to occur in these regions. We also performed DFEM to directly investigate the potential contribution of the striated region (described in Fig. 1F) during an impact event, by imposing a higher modulus in this location to account for the observed changes in chitin fiber orientation. These simulations revealed that this circumferential band-like structure prevents lateral deformation of the club,

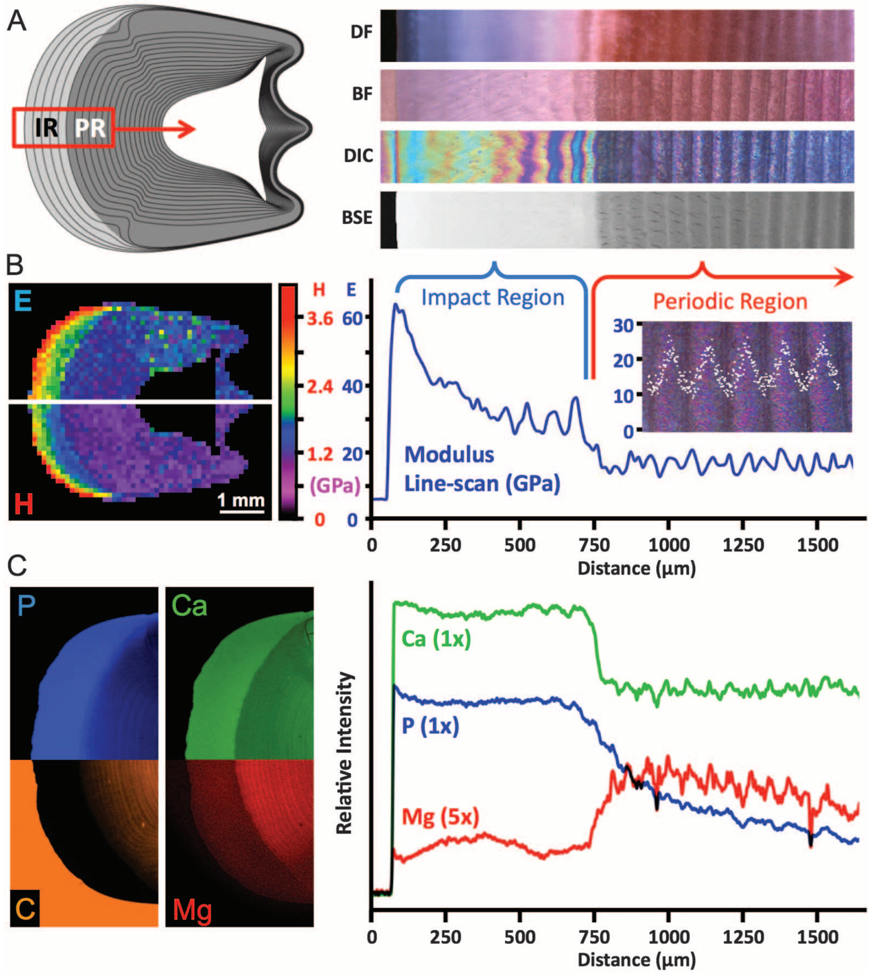


**Fig. 2.** Micromechanical and compositional variability in the stomatopod dactyl club. All of the images and plots in the right-hand column of the figure correspond to parallel analyses through the same region of a dry specimen, facilitating direct comparisons between ultrastructure, micromechanics, and elemental composition. (**A**) Diagrammatic backscattered electron micrograph through the dactyl club indicating the locations of the impact region (IR) and the periodic region (PR) and the corresponding optical [darkfield (DF), brightfield (BF), and differential interference contrast (DIC)], and backscattered scanning electron (BSE) micrographs of the area boxed in red. (**B**) Large-area nanoindentation [elastic modulus (E) and hardness (H)] map of the dactyl club and a corresponding line scan, including a high-resolution plot through five superlayers; periodicity: ~75 µm overlayed on a corresponding DIC micrograph. (**C**) EDS maps and line scans showing the nonuniform elemental distributions in the periodic and impact regions (the Mg concentration EDS data have been expanded by a factor of 5 relative to the Ca and P concentrations).

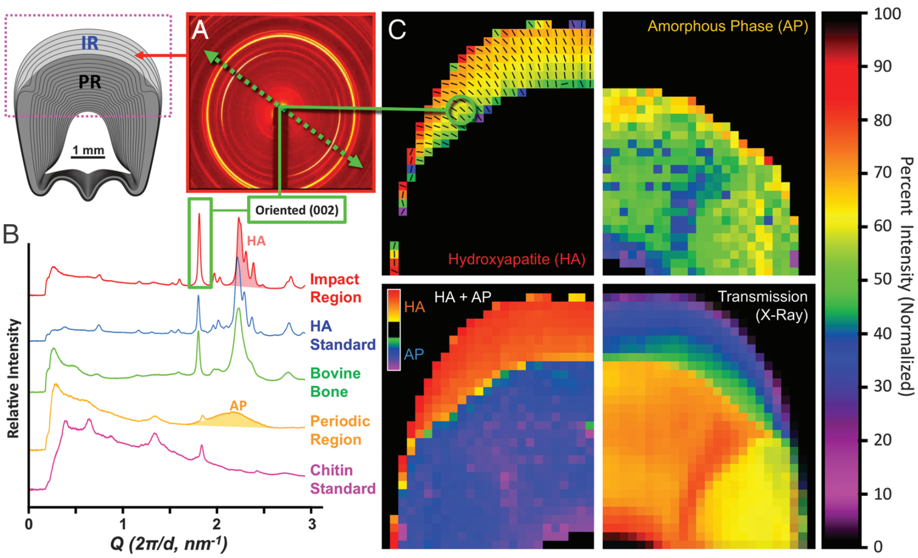


**Fig. 3.** Synchrotron x-ray diffraction (XRD) analysis and distribution of various mineral phases in the dactyl club. (**A**) A single diffractogram taken from the impact region (IR) of a transverse cross section. The preferred orientation of the hydroxyapatite (HA) crystal's *c* axis (green arrows) is placed at the peak intensity of the HA (002) reflection. (**B**) Representative XRD patterns from the impact (IR) and periodic regions (PR) compared against standards. The colored areas of the impact and periodic region diffraction patterns were used to estimate the mineral concentrations shown in (C). (**C**) Mineral concentration maps for the HA and the amorphous phases (each of the four synchrotron maps measures ~2.5 mm across). The sloped black lines denote the preferred orientation of the HA *c* axis (002). A composite mineral concentration map (lower left) confirms that both maps measured the same boundary between phases. An x-ray transmission map (lower right) correlates inversely with mineral concentration.

hence restricting the maximum principal strain within the periodic region and locally reducing the crack opening displacement of a potential propagating crack, and consequentially limiting its driving force (*26*). Furthermore, these simulations indicate that the highly aligned chitin fiber bundles of the striated region, which are oriented perpendicular to the transverse cross section (Fig. 1F), may provide additional compressive and torsional stiffness during compression of the club.

**Mechanistic origins of toughness and damage tolerance.** Although DFEM simulations provide important insight into the stress distribution, macroscopic structural integrity, and potential sites of microcrack nucleation, they do not take into account the complex microstructural features of the dactyl club. To correlate these features with the observed damage tolerance and the high toughness of the club, a micromechanical analysis must also be considered. Intuitively, it is not surprising to find a hard outermost layer in a structure employed for high-energy impacts as this design is widely used for mechanically active (*27*, *28*) or protective (*29*) hard tissues. In the dactyl club, this enhanced surface hardness is achieved by a higher degree of crystallinity, combined with a preferred orientation of the hydroxyapatite crystallites near the impact surface (Fig. 3C, upper left), which imparts additional rigidity due to the greater hardness and stiffness of the hydroxyapatite basal versus prismatic faces (*30*). In addition to this first line of defense, its microstructural complexity imparts the club with several mechanisms against catastrophic failure that are detailed in Fig. 5D.

Although DFEM suggests that internal cracks are likely to nucleate beneath the impact region, the helicoidal architecture provides several toughening mechanisms that hinder catastrophic propagation of such cracks (Fig. 5D). Charge contrast secondary electron micrographs of coronal cross sections (Fig. 4F) illustrate the tendency of cracks to nest volumetrically within the periodic region between the chitin fibers. In three dimensions, this can be represented as a helicoidal fracture pattern propagating between layers, with a rotating crack front that remains parallel to the fibers without severing them. We confirmed this hypothesis by modeling a coronal cross section of a helicoidal stack of fibers curved around a spherical core (Fig. 4H and fig. S2), which results in the distinctive double spiral-like motif shown in Fig. 4, G and H. This model precisely reproduces the charge contrast fractographs, providing strong evidence that cracks predominantly propagate helicoidally between the chitin fibers. One key implication is that this pattern creates a much larger surface area per unit crack length in the main direction of propagation, hence amplifying the total energy dissipated during impact and crack propagation, a behavior that has also been observed in engineered helicoidal composites (*31*).

When a crack deviates from its helicoidal path and propagates straight into neighboring layers, it encounters an elastic modulus oscillation due to their anisotropic stiffness. This oscillation period is on the order of 75 μm, and the relative thickness of stiff ($E_{max}$) and compliant ($E_{min}$) layers depends on the angle of the crack front relative to the helicoid axis. As shown by Fratzl *et al.* (*32*), this oscillation provides an additional protection against damage. Indeed, the *J*-integral crack driving force, $J_{far}$, surrounding the crack is shielded at the tip, $J_{tip} = J_{far} \cdot f_{inh}$, where $f_{inh}$ is the shielding factor, which directly depends on the relative thickness and modulus ratios $\rho = E_{max}/E_{min}$. We used our nanoindentation line-scan profiles to fit the oscillation wavelength and modulus ratio ρ, and applied this analysis to the club (fig. S4). These results suggest that crack propagation across layers is hampered by the modulus oscillation, which improves the damage tolerance with an efficiency that depends on the crack propagation direction relative to the chitin fiber orientation.

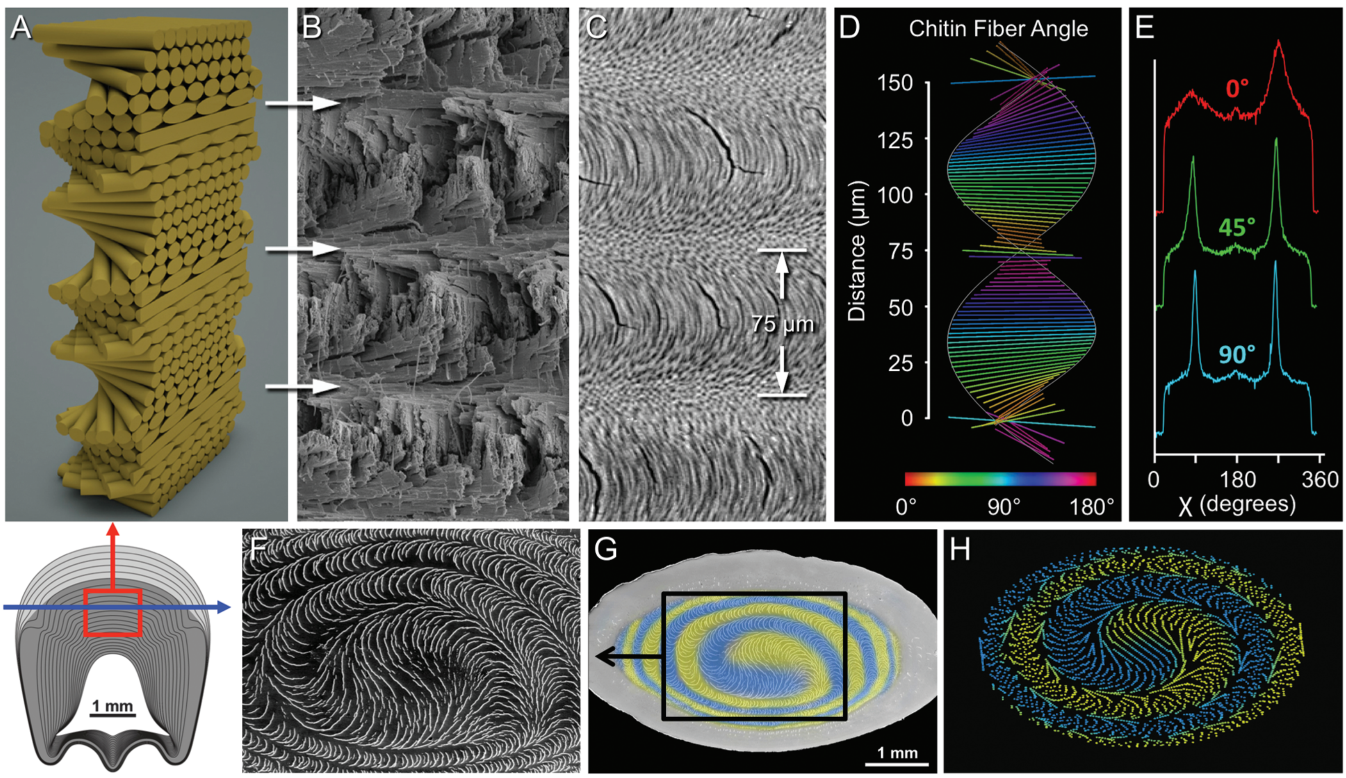


**Fig. 4.** Chitin fibril helicoidal structural motif within the periodic region (with periodicity: ~75 μm). Comparisons between a generalized three-dimensional model of a helicoid (**A**) with an SEM fractograph (**B**) and a polished surface from a transverse cross section (**C**). (**D**) A visualization of the chitin fiber orientations from the x-ray scattering analysis of 92 separate diffractograms obtained through two superlayers. (**E**) Three representative χ plots of the α-chitin (110) reflection used to calculate fiber angles. The plots show changes in χ across the range of angles between each chitin fiber bundle and the x-ray beam. A charge contrast scanning electron micrograph from a damaged coronal cross section (**F**) with false color (**G**) and a model of a helicoidal slice (**H**), which accurately reproduces the fracture patterns.

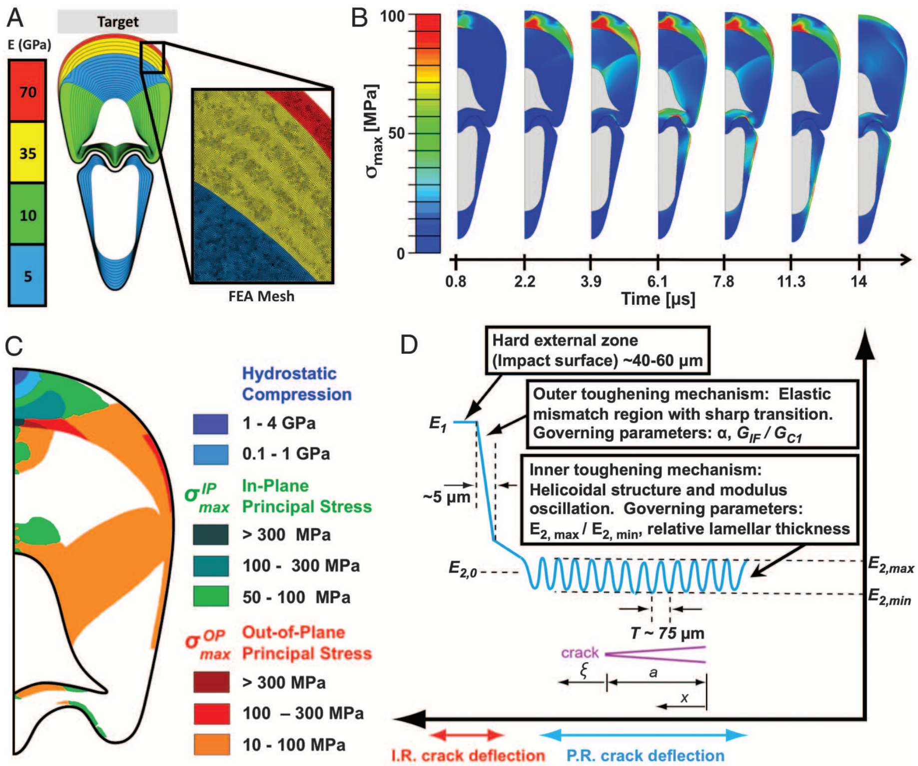


**Fig. 5.** Dynamic finite element analysis (DFEA) and micromechanical modeling. (**A**) Geometry of the dactyl club/propodus system striking a target at 20 m/s. Color-coding corresponds to the different elastic properties and mass densities used for DFEA simulations (data obtained from nanomenchanical characterization of hydrated specimens and synchrotron x-ray transmission studies). (**B**) Evolution of the maximum principal stress $\sigma_{max}$ during the impact event until the propagating pressure wave reaches the end of the propodus. (**C**) Maximal principal stresses within the dactyl club at ~2 μs after impact. (**D**) Toughening strategies of the dactyl club: (i) hard outer layer for maximum impact force; (ii) modulus transitional domain for crack deflection between the impact surface and the bulk of the impact region; (iii) periodic region with helicoidal pattern and modulus oscillation for crack shielding. $a$, crack length; $x$, coordinate perpendicular to the crack front propagation; $\xi$, relative coordinate ahead of the crack tip in the periodic region ($\xi = x - a$); $E(x)$, elastic modulus oscillation.

This prediction was supported by the observed presence of microcracks crossing the helicoid and arresting within a few layers in scanning electron micrographs of transverse polished cross sections (Fig. 4C).

A final protective mechanism against catastrophic fracture is provided by the sharp transition between the impact surface and the bulk of the impact region. If a crack approaches the impact surface, it encounters an elastic modulus mismatch. A crack propagating from a more compliant region ($E_2$) can either be deflected at the interface or propagated through the stiffer region ($E_1$). This tendency depends on the Dundurs' parameter $\alpha = (E_1 - E_2)/(E_1 + E_2)$ (modulus mismatch) and on the fracture toughness of the interface, $G_{IF}$, and of the stiff material, $G_{C1}$. The propensity for a crack to exhibit either of these regimes can be expressed as a critical ($G_{IF}/G_{C1}$ versus $\alpha$) curve (*33*). The $\alpha$ value at this interface beneath the impact surface is 0.33 [appreciably smaller than 0.52 of dentin/enamel junction in mammalian teeth (*34*)], corresponding to a critical $G_{IF}/G_{C1}$ of ~0.35 (*33*). Hence, if $G_{IF}$ is less than 35% of $G_{C1}$, crack deflection occurs at the interface. Such a mechanism has important implications, because the crack-tip stress amplification is greatly reduced when debonding occurs (*35*). If, however, $G_{IF} > 0.35 G_{C1}$, the impinging crack is likely to penetrate through the hard impact surface, which would substantially affect the club's structural integrity. Charge-contrast scanning electron micrographs (fig. S6) indicate that cracks remain mostly contained within the periodic region, with evidence of deflection within the impact region, implying that the $G_{IF}/G_{C1}$ ratio successfully prevents cracks from reaching the club's outer surface. Given the complexity of the club's microstructure, other dissipative mechanisms at the micro- and nanoscale must also contribute to its toughening. As in other mineralized biocomposites, these could include microcracking at the crack-tip process zone, crack bridging from mineralized chitin fibers, or crack deflection at interfaces (*36*), as well as time-dependent mechanisms, which will all be amplified by the helicoidal crack pattern.

**Conclusion.** Our studies show that the stomatopod dactyl club represents a notable departure from previously studied damage-tolerant biological composites, in that it is specifically employed for high-velocity offensive strikes. Our structural investigations, coupled with nanomechanical characterization and finite element simulations, have shown that the club consists of several microstructural features that permit the infliction of crippling impacts while simultaneously minimizing internal damage within the club. These characteristics include a pitch-graded helicoidal architecture constructed from mineralized chitin fibers that can dissipate the energy released by propagating microcracks; an oscillating elastic modulus that provides further shielding against catastrophic crack propagation; a modulus mismatch in the impact region that acts as a crack deflector near the impact surface; and an ultrahard outer layer correlated with a high level of mineralization and a radial organization of apatitic crystallites. The structural lessons gained from the study of this multiphase biological composite could thus provide important design insights into the fabrication of tough ceramic/organic hybrid materials in structural applications where components are subjected to intense repetitive loading.

### References and Notes


1. F. R. Schram, *J. Paleontol.* **81**, 895 (2007).
2. T. W. Cronin, N. J. Marshall, *Nature* **339**, 137 (1989).
3. R. L. Caldwell, H. Dingle, *Naturwissenschaften* **62**, 214 (1975).
4. J. R. A. Taylor, S. N. Patek, *J. Exp. Biol.* **213**, 3496 (2010).
5. T. Claverie, E. Chan, S. N. Patek, *Evolution* **65**, 443 (2011).
6. F. C. Lukis, *Mag. Nat. Hist. J. Zool. Bot. Mineral. Geol. Meteorol.* **8**, 459 (1835).
7. J. W. C. Dunlop, P. Fratzl, *Annu. Rev. Mater. Res.* **40**, 1 (2010).
8. S. Deville, E. Saiz, R. K. Nalla, A. P. Tomsia, *Science* **311**, 515 (2006).
9. A. H. Heuer *et al.*, *Science* **255**, 1098 (1992).
10. S. T. Ahyong, C. Harling, *Aust. J. Zool.* **48**, 607 (2000).
11. S. N. Patek, R. L. Caldwell, *J. Exp. Biol.* **208**, 3655 (2005).
12. M. L. Reaka, *J. Morphol.* **146**, 55 (1975).
13. J. D. Currey, A. Nash, W. Bonfield, *J. Mater.* **17**, 1939 (1982).
14. C. Ooi, M. Hamdi, S. Ramesh, *Ceram. Int.* **33**, 1171 (2007).
15. G. Luquet, F. Marin, *C. R. Palevol* **3**, 515 (2004).
16. E. Loste, R. M. Wilson, R. Seshadri, F. C. Meldrum, *J. Cryst. Growth* **254**, 206 (2003).
17. Y. Politi *et al.*, *J. Mater.* **22**, 161 (2010).
18. L. Cheng, L. Wang, A. M. Karlsson, *J. Mater. Res.* **23**, 2854 (2008).
19. S. Weiner, T. Arad, I. Sabanay, W. Traub, *Bone* **20**, 509 (1997).
20. R. Roer, R. Dillaman, *Am. Zool.* **24**, 893 (1984).
21. A. Al-Sawalmih *et al.*, *Adv. Funct. Mater.* **18**, 3307 (2008).
22. R. Minke, J. Blackwell, *J. Mol. Biol.* **120**, 167 (1978).
23. H. Lichtenegger, M. Müller, O. Paris, C. Riekel, P. Fratzl, *J. Appl. Cryst.* **32**, 1127 (1999).
24. O. Paris, M. Muller, *Nucl. Instrum. Methods Phys. Res. B* **200**, 390 (2003).
25. N. E. Dowling, *Mechanical Behavior of Matererials* (Prentice Hall, NJ, ed. 3, 2006).
26. C. F. Shih, *J. Mech. Phys. Solids* **29**, 305 (1981).
27. S. Habelitz, G. W. Marshall Jr., M. Balooch, S. J. Marshall, *J. Biomech.* **35**, 995 (2002).
28. J. C. Weaver *et al.*, *Mater. Today* **13**, 42 (2010).
29. B. J. B. Bruet, J. Song, M. C. Boyce, C. Ortiz, *Nat. Mater.* **7**, 748 (2008).
30. B. Viswanath, R. Raghavan, U. Ramamurty, N. Ravishankar, *Scr. Mater.* **57**, 361 (2007).

31. T. Apichattrabrut, K. Ravi-Chandar, *Mech. Adv. Mater. Structures* **13**, 61 (2006).
32. P. Fratzl, H. S. Gupta, F. D. Fisher, O. Kolednik, *Adv. Mater.* **19**, 2657 (2007).
33. H. Ming-Yuan, J. W. Hutchinson, *Int. J. Solids Struct.* **25**, 1053 (1989).
34. V. Imbeni *et al.*, *Nat. Mater.* **4**, 229 (2005).
35. K. S. Chan, M. Y. He, J. W. Hutchinson, *Mater. Sci. Eng. A* **167**, 57 (1993).
36. R. Wang, H. S. Gupta, *Annu. Rev. Mater. Res.* **41**, 41 (2011).
37. W. K. Brooks, *Report on the Scientific Results of the Exploring Voyage of the H.M.S. Challenger*, vol. 45, *Stomatopoda* (Neill and Co., Edinburgh, 1886).

**Acknowledgments:** We thank J. Vieregge, R. Nay, J. Rawlins, and S. Amini for technical assistance and S. Baron, P. Allen, and D. McLaren for specimen photography and graphic design. This research was supported by grants from the National Science Foundation, DMR-0906770 (D.K.), the Singapore National Research Foundation (NRF) through a NRF Fellowship (A.M.), and Air Force Office of Scientific Research (AFOSR-FA9550-10-1-0322 and AFOSR-FA9550-10-1-0209). Brookhaven National Laboratory is supported under U.S. Department of Energy Contract DE-AC02-98CH10886.

**Supplementary Materials**
www.sciencemag.org/cgi/content/full/336/6086/1275/DC1
Materials and Methods
Figs. S1 to S6
References (*38–40*)

5 January 2012; accepted 19 April 2012
10.1126/science.1218764



# Quantum Information Storage for over 180 s Using Donor Spins in a $^{28}$Si "Semiconductor Vacuum"

M. Steger,[1] K. Saeedi,[1] M. L. W. Thewalt,[1]* J. J. L. Morton,[2] H. Riemann,[3] N. V. Abrosimov,[3] P. Becker,[4] H.-J. Pohl[5]

A quantum computer requires systems that are isolated from their environment, but can be integrated into devices, and whose states can be measured with high accuracy. Nuclear spins in solids promise long coherence lifetimes, but they are difficult to initialize into known states and to detect with high sensitivity. We show how the distinctive optical properties of enriched $^{28}$Si enable the use of hyperfine-resolved optical transitions, as previously applied to great effect for isolated atoms and ions in vacuum. Together with efficient Auger photoionization, these resolved hyperfine transitions permit rapid nuclear hyperpolarization and electrical spin-readout. We combine these techniques to detect nuclear magnetic resonance from dilute $^{31}$P in the purest available sample of $^{28}$Si, at concentrations inaccessible to conventional measurements, measuring a solid-state coherence time of over 180 seconds.

If computers could store and process quantum information, they could solve a host of problems that are intractable with even the fastest of modern supercomputers. Among the many different physical systems proposed to implement such a quantum computer (*1*), there is a trade-off between the low error rates and exquisite control exhibited by quantum systems in high-vacuum environments (*2*) versus the inherent scalability and device compatibility offered by solid-state systems (*3*). One promising solution is to identify suitable ultrapure materials offering a vacuumlike environment to quantum systems residing within. Motivated by its central role in conventional electronics, silicon has become one of the most highly purified materials, with impurity and defect densities typically measured in parts per billion or below. Even the isotopic variation in silicon (which exists as $^{28}$Si, $^{29}$Si, and $^{30}$Si, with only $^{29}$Si having nonzero nuclear spin) can be addressed, with 99.995% $^{28}$Si material produced as part of a project to redefine the kilogram (*4*). Silicon therefore offers the potential to bridge the gap between these approaches to quantum information processing: providing

[1]Department of Physics, Simon Fraser University, Burnaby, BC V5A 1S6, Canada. [2]Department of Materials, Oxford University, Oxford OX1 3PH, UK. [3]Leibniz-Institut für Kristallzüchtung, 12489 Berlin, Germany. [4]PTB (Physikalisch-Technische Bundesanstalt) Braunschweig, 38116 Braunschweig, Germany. [5]Vitcon Projectconsult GmbH, 07745 Jena, Germany.

*To whom correspondence should be addressed. E-mail: thewalt@sfu.ca

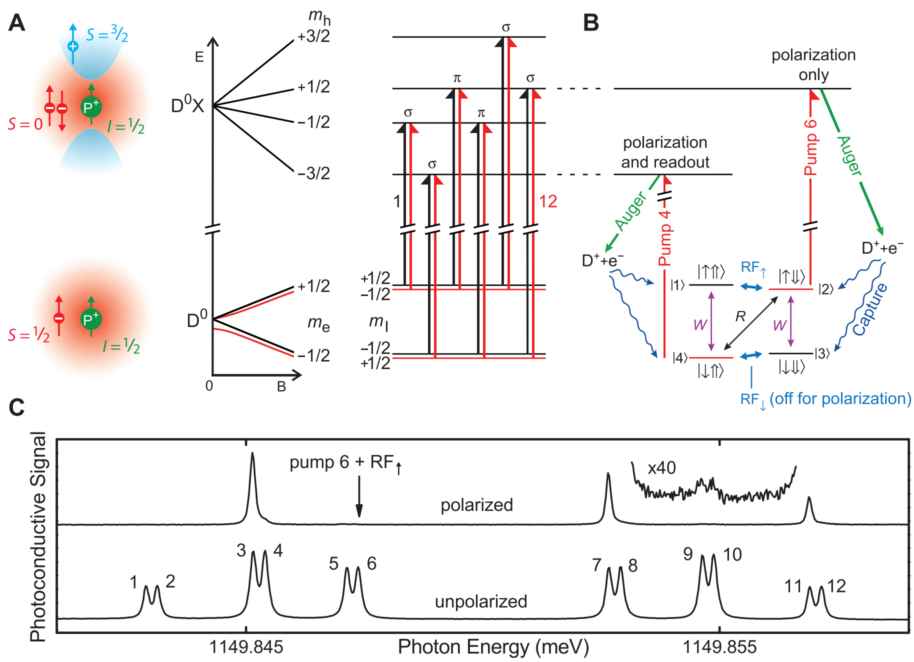


**Fig. 1.** Spin-selective creation of the D$^0$X is used to polarize and read out the $^{31}$P nuclear spin. (**A**) The ground states of the D$^0$X and D$^0$ and their splittings under a magnetic field, showing the origin of the 12 dipole-allowed absorption transitions, labeled from 1 to 12 in order of increasing energy (*E*). (**B**) The hyperpolarization mechanism used here polarizes D$^0$ into hyperfine state $|3\rangle$, with polarizing laser on line 6, readout laser on line 4, and RF applied at RF$_\uparrow$. The single and double arrows denote the electron and nuclear spins, respectively. (**C**) Photoconductivity spectra at $T$ = 4.2 K and $\boldsymbol{B}$ = 845 G, for the largely unpolarized equilibrium case (bottom) and using the hyperpolarization scheme (top). The relative intensities of lines 3, 4, 9, and 10 give directly the relative populations of D$^0$ states $|3\rangle$, $|4\rangle$, $|1\rangle$, and $|2\rangle$, respectively.

**The Stomatopod Dactyl Club: A Formidable Damage-Tolerant Biological Hammer**
James C. Weaver *et al.*
*Science* **336**, 1275 (2012);
DOI: 10.1126/science.1218764